

Disruption of IRE1α through its kinase domain attenuates multiple myeloma

Jonathan M Harnoss, Adrien Le Thomas, Anna Shemorry, Scot A Marsters, David S Lawrence, Min Lu, Yung-Chia Ariel Chen, Jing Qing, Klara Totpal, David Kan, et al.

▶ **To cite this version:**

Jonathan M Harnoss, Adrien Le Thomas, Anna Shemorry, Scot A Marsters, David S Lawrence, et al.. Disruption of IRE1α through its kinase domain attenuates multiple myeloma. Proceedings of the National Academy of Sciences of the United States of America, 2019, pp.201906999. 10.1073/pnas.1906999116 . inserm-02265831

HAL Id: inserm-02265831

https://inserm.hal.science/inserm-02265831

Submitted on 12 Aug 2019

HAL is a multi-disciplinary open access archive for the deposit and dissemination of scientific research documents, whether they are published or not. The documents may come from teaching and research institutions in France or abroad, or from public or private research centers.

L'archive ouverte pluridisciplinaire **HAL**, est destinée au dépôt et à la diffusion de documents scientifiques de niveau recherche, publiés ou non, émanant des établissements d'enseignement et de recherche français ou étrangers, des laboratoires publics ou privés.

Disruption of IRE1α through its kinase domain attenuates multiple myeloma

Jonathan M. Harnoss[a], Adrien Le Thomas[a], Anna Shemorry[a], Scot A. Marsters[a], David A. Lawrence[a], Min Lu[a,1], Yung-Chia Ariel Chen[a,2], Jing Qing[a], Klara Totpal[b], David Kan[b], Ehud Segal[b], Mark Merchant[b], Mike Reichelt[c], Heidi Ackerly Wallweber[d], Weiru Wang[d], Kevin Clark[e], Susan Kaufman[e], Maureen H. Beresini[e], Steven T. Laing[c], Wendy Sandoval[f], Maria Lorenzo[g], Jiansheng Wu[g], Justin Ly[h], Tom De Bruyn[h], Amy Heidersbach[i], Benjamin Haley[i], Alvin Gogineni[j], Robby M. Weimer[j], Dong Lee[k,2], Marie-Gabrielle Braun[l], Joachim Rudolph[l], Michael J. VanWyngarden[m], Daniel W. Sherbenou[m], Patricia Gomez-Bougie[n,o], Martine Amiot[n,o], Diego Acosta-Alvear[p,q,3], Peter Walter[p,q], and Avi Ashkenazi[a,4]

[a]Cancer Immunology, Genentech, Inc., South San Francisco, CA 94080; [b]Translational Oncology, Genentech, Inc., South San Francisco, CA 94080; [c]Pathology, Genentech, Inc., South San Francisco, CA 94080; [d]Structural Biology, Genentech, Inc., South San Francisco, CA 94080; [e]Biochemical and Cellular Pharmacology, Genentech, Inc., South San Francisco, CA 94080; [f]Microchemistry, Proteomics and Lipidomics, Genentech, Inc., South San Francisco, CA 94080; [g]Protein Chemistry, Genentech, Inc., South San Francisco, CA 94080; [h]Drug Metabolism and Pharmacokinetics, Genentech, Inc., South San Francisco, CA 94080; [i]Molecular Biology, Genentech, Inc., South San Francisco, CA 94080; [j]Biomolecular Imaging, Genentech, Inc., South San Francisco, CA 94080; [k]Safety Assessment, Genentech, Inc., South San Francisco, CA 94080; [l]Discovery Chemistry, Genentech, Inc., South San Francisco, CA 94080; [m]Division of Hematology, Department of Medicine, University of Colorado Cancer Center, Aurora, CO 80045; [n]Centre de Recherche en Cancérologie et Immunologie Nantes-Angers, INSERM, CNRS, Université d'Angers, Université de Nantes, BP 70721 Nantes, France; [o]Service d'Hématologie Clinique, Unité d'Investigation Clinique, Centre Hospitalier Universitaire, BP 70721 Nantes, France; [p]Department of Biochemistry and Biophysics, University of California, San Francisco, CA 94143; and [q]Howard Hughes Medical Institute, University of California, San Francisco, CA 94143

Edited by Hidde L. Ploegh, Boston Children's Hospital, Boston, MA, and approved July 5, 2019 (received for review May 12, 2019)

Multiple myeloma (MM) arises from malignant immunoglobulin (Ig)-secreting plasma cells and remains an incurable, often lethal disease despite therapeutic advances. The unfolded-protein response sensor IRE1α supports protein secretion by deploying a kinase–endoribonuclease module to activate the transcription factor XBP1s. MM cells may co-opt the IRE1α–XBP1s pathway; however, the validity of IRE1α as a potential MM therapeutic target is controversial. Genetic disruption of IRE1α or XBP1s, or pharmacologic IRE1α kinase inhibition, attenuated subcutaneous or orthometastatic growth of MM tumors in mice and augmented efficacy of two established frontline antimyeloma agents, bortezomib and lenalidomide. Mechanistically, IRE1α perturbation inhibited expression of key components of the endoplasmic reticulum-associated degradation machinery, as well as secretion of Ig light chains and of cytokines and chemokines known to promote MM growth. Selective IRE1α kinase inhibition reduced viability of CD138$^+$ plasma cells while sparing CD138$^-$ cells derived from bone marrows of newly diagnosed or posttreatment-relapsed MM patients, in both US- and European Union-based cohorts. Effective IRE1α inhibition preserved glucose-induced insulin secretion by pancreatic microislets and viability of primary hepatocytes in vitro, as well as normal tissue homeostasis in mice. These results establish a strong rationale for developing kinase-directed inhibitors of IRE1α for MM therapy.

multiple myeloma | endoplasmic reticulum stress | unfolded protein response | inositol-requiring enzyme 1 | kinase inhibitors

Multiple myeloma (MM) is the second most common human hematologic cancer. It carries a lifetime risk of 0.7% and occurs mainly in older individuals. MM is caused by bone marrow infiltration by malignant, monoclonal immunoglobulin (Ig)-secreting plasma cells (1). Despite significant therapeutic advances—including proteasome inhibitors (PIs), immunomodulatory agents (IMiDs), and anti-CD38 antibodies—MM remains mainly incurable, with acquired resistance to all available agents, and a 5-y survival rate of 49% (2). Considering the growth of aging populations in many countries, there is an urgent unmet need for development of novel MM therapies.

The endoplasmic reticulum (ER) ensures precise folding of newly synthesized secretory proteins. Upon elevated cellular demand for protein secretion—for example, when mature B cells differentiate into Ig-secreting plasma cells—insufficient ER capacity causes accumulation of unfolded proteins (UPs) in the ER lumen. This activates a sensing–signaling network dubbed the UP response (UPR) to orchestrate ER adaptation and reestablish homeostasis (3–6). The mammalian UPR employs three pivotal ER-resident transmembrane sensors: inositol-requiring enzyme

Significance

Multiple myeloma (MM) is a lethal malignancy arising from plasma cells. MM cells experience endoplasmic reticulum (ER) stress due to immunoglobulin hyperproduction. The ER-resident sensor IRE1α mitigates ER stress by expanding protein-folding and secretion capacity, while supporting proteasomal degradation of ER misfolded proteins. IRE1α elaborates these functions by deploying a cytoplasmic kinase–RNase module to activate the transcription factor XBP1s. Although IRE1α has been implicated in MM, its validity as a potential therapeutic target—particularly as a kinase—has been unclear. Using genetic and pharmacologic disruption, we demonstrate that the IRE1α–XBP1s pathway is critical for MM tumor growth. We further show that the kinase domain of IRE1α is an effective and safe potential small-molecule target for MM therapy.

Author contributions: J.M.H., A.L.T., A.S., S.A.M., D.A.L., M. Lu, Y.-C.A.C., H.A.W., W.W., A.H., B.H., A.G., R.M.W., D.L., M.-G.B., J.R., M.J.V., D.W.S., P.G.-B., M.A., D.A.-A., P.W., and A.A. designed research; J.M.H., A.L.T., A.S., S.A.M., D.A.L., M. Lu, Y.-C.A.C., J.Q., K.T., D.K., E.S., M.M., M.R., H.A.W., W.W., K.C., S.K., M.H.B., S.T.L., W.S., M. Lorenzo, J.W., J.L., T.D.B., A.H., B.H., A.G., R.M.W., D.L., M.-G.B., J.R., M.J.V., D.W.S., P.G.-B., and M.A. performed research; J.Q., D.A.-A., and P.W. contributed new reagents/analytic tools; J.M.H., A.L.T., A.S., S.A.M., D.A.L., M. Lu, Y.-C.A.C., M.R., H.A.W., W.W., S.T.L., A.G., R.M.W., M.-G.B., J.R., M.J.V., D.W.S., P.G.-B., M.A., D.A.-A., P.W., and A.A. analyzed data; and J.M.H. and A.A. wrote the paper.

Conflict of interest statement: J.M.H., A.L.T., A.S., S.A.M., D.A.L., M. Lu, Y.-C.A.C., J.Q., K.T., D.K., E.S., M.M., M.R., H.A.W., W.W., K.C., S.K., M.H.B., S.T.L., W.S., M. Lorenzo, J.W., J.L., T.D.B., A.H., B.H., A.G., R.M.W., D.L., M.-G.B., J.R., and A.A. were employees of Genentech, Inc. during performance of this work.

This article is a PNAS Direct Submission.

This open access article is distributed under Creative Commons Attribution-NonCommercial-NoDerivatives License 4.0 (CC BY-NC-ND).

[1]Present address: Agios Pharmaceuticals, Cambridge, MA 02139.

[2]Present address: Revolution Medicines, Redwood City, CA 94063.

[3]Present address: Department of Molecular, Cellular and Developmental Biology, University of California, Santa Barbara, CA 93106.

[4]To whom correspondence may be addressed. Email: aa@gene.com.

This article contains supporting information online at www.pnas.org/lookup/suppl/doi:10.1073/pnas.1906999116/-/DCSupplemental.

1 α (IRE1α), protein kinase-like ER kinase (PERK), and activating transcription factor-6 (ATF6). UP detection by the ER-luminal domain of each sensor engages the cytoplasmic moiety to adjust the ER's protein-folding, secretory, and degradative capacities and alleviate ER stress. If adaptation fails and stress becomes overwhelming, the UPR triggers apoptosis (7). Conserved from yeast to primates, IRE1α harbors lumenal, transmembrane, and cytosolic regions: The cytoplasmic part contains a serine/threonine kinase domain and a tandem endoribonuclease (RNase) module (8, 9). IRE1α activation involves oligomerization, kinase transautophosphorylation, and RNase activation (9–12). The RNase cleaves the mRNA encoding unspliced X-box protein 1 (XBP1u), removing a 26-nucleotide intron, and triggering RtcB -mediated ligation of spliced XBP1 (XBP1s) (3–5, 13). The XBP1s protein acts as a transcription factor that stimulates multiple genes including chaperones and disulfide isomerases that facilitate protein folding (14–16). XBP1s also induces key components of ER-associated degradation (ERAD), which promotes retrotranslocation of UPs into the cytoplasm, followed by their ubiquitination and proteasomal disposal (14, 17). An alternative IRE1α activity—termed regulated IRE1α-dependent decay (RIDD)—cleaves ER-associated mRNAs to abate translational load (18, 19) and suppress apoptosis (20, 21).

Because plasma–cell differentiation requires IRE1α and XBP1s (22–24), and because cancer cells often co-opt normal stress-response pathways to support malignant growth in hostile microenvironments (25), it has been proposed that the IRE1α–XBP1s pathway may represent a therapeutically useful vulnerability in MM (26–28). Supporting this hypothesis, transgenic expression of XBP1s in B cells drove MM-like pathology in mice (29), and high XBP1s levels correlated with worse prognosis in MM patients (30). XBP1s depletion by short hairpin RNAs (shRNAs) attenuated growth of certain MM cell lines in vitro, and small-molecule inhibition of IRE1α's RNase with salicylaldehyde compounds modestly attenuated human MM xenograft growth in mice (31, 32). Standard-of-care agents such as PIs are effective in MM therapy likely because their inhibition of the 26S proteasome creates a backlog of ERAD substrates that cannot be efficiently degraded, thereby exacerbating ER stress (33). However, lower XBP1s levels in MM cells correlated with PI resistance (33, 34). Furthermore, although IRE1α kinase inhibition blocked XBP1s production, it failed to attenuate MM cell growth under standard tissue culture conditions in vitro (35). A significant caveat of salicylaldehyde-based IRE1α RNase inhibitors is that the selectivity of such compounds for IRE1α is difficult to ascertain; indeed, recent work reveals that one of these compounds acts as an antioxidant due to off-target activity (36). In addition, because XBP1s depletion drives hyperphosphorylation of IRE1α (20, 37), alternative, XBP1s-independent IRE1α functions—for example, activation of c-Jun N-terminal kinase (JNK) (38)—also may impact MM cells. Whether IRE1α can be targeted effectively and safely via its kinase domain to inhibit MM tumor growth under conditions that more faithfully represent this disease remains an open question.

Our results demonstrate that the IRE1α–XBP1s pathway plays a critical role in supporting MM cell growth in vitro in 3D culture settings, as well as in vivo in subcutaneous (s.c.) as well as orthometastatic tumor xenografts. Furthermore, selective small-molecule IRE1α kinase inhibition reduced viability of malignant MM cells in patient-derived bone marrows yet spared accompanying normal cells; it also preserved insulin secretion by pancreatic microislets and viability of primary hepatocytes in vitro and was well tolerated at therapeutically effective doses in mice. Together, these findings provide a compelling rationale for targeting IRE1α via its kinase domain in MM.

Results

Depletion of IRE1α by shRNAs Attenuates 3D Growth of MM Cell Lines. Interrogation of the cancer cell line encyclopedia (CCLE) RNA sequencing (RNAseq) dataset (Broad Institute) demonstrated that MM cell lines express higher messenger RNA (mRNA) levels of IRE1α than all other cancer types (*SI Appendix*, Fig. S1*A*). Further analysis of 12 human MM cell lines by immunoblot (IB) revealed abundant IRE1α protein, often in conjunction with detectable XBP1s protein (Fig. 1*A*), suggesting frequent IRE1α–XBP1s pathway activation in MM cells. To investigate the importance

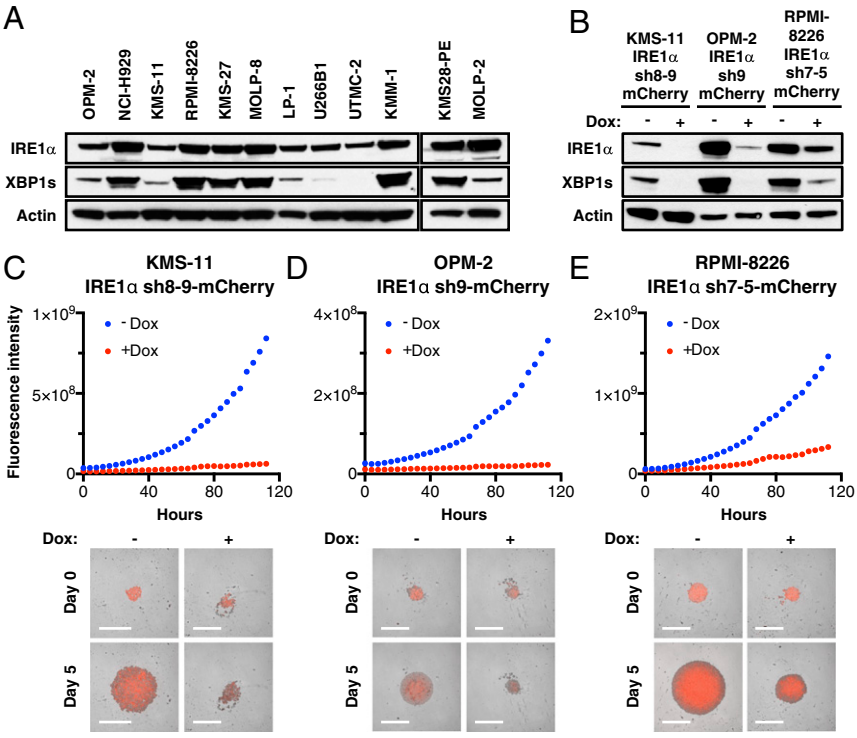


Fig. 1. Expression of IRE1α in MM cell lines and effect of its depletion on spheroid 3D growth. (*A*) Twelve human MM cell lines were analyzed by immunoblot (IB) for protein levels of IRE1α and XBP1s. (*B–F*) KMS-11, OPM-2, and RPMI-8226 MM cells were stably transfected with a plasmid encoding doxycycline (Dox)-inducible shRNAs against IRE1α together with a plasmid encoding mCherry. Cells were incubated in the absence or presence of Dox (0.5 μg/mL) for 3 d, seeded on ultralow adhesion (ULA) plates, centrifuged to form single spheroids, and analyzed by IB for indicated proteins (*B*) or for growth based on mCherry fluorescence using an Incucyte instrument. (*C–E*, *Lower*) Representative images of indicated MM cells grown as single spheroids in ULA plates. (Scale bars, 800 μm.)

of IRE1α for MM cell growth, we first used a doxycycline (Dox)-inducible shRNA-based knockdown approach. As expected, Dox-driven anti-IRE1α shRNA induction markedly decreased IRE1α and XBP1s protein levels in KMS-11, OPM-2, and RPMI-8226 MM cells (Fig. 1*B*). Importantly, Dox-induced IRE1α depletion profoundly inhibited proliferation of these three cell lines upon 3D growth as single spheroids on ultralow attachment (ULA) plates, as evident by fluorescence imaging (Fig. 1 *C–E*). In contrast, Dox treatment of the parental KMS-11 cells did not alter growth (*SI Appendix*, Fig. S1 *B* and *C*). IRE1α knockdown also inhibited 3D growth of KMS-11 cells as multiple spheroids on Matrigel, as determined via an Incucyte S3 instrument (*SI Appendix*, Fig. S1 *D* and *E*). While Dox treatment did not affect viability, as measured by CellTiter-Glo, of parental KMS-11 cells cultured on Matrigel, Dox-induced IRE1α depletion led to a substantial loss of viability (*SI Appendix*, Fig. S1 *F–H*). Thus, three genetically diverse MM cell lines (39) displayed significant dependence on IRE1α for 3D growth—a modality that more faithfully reflects in vivo tumor settings than the conventional 2D culture used in earlier work (35).

Genetic Disruption of IRE1α or XBP1s Attenuates Growth of s.c. Human MM Xenografts. We next disrupted IRE1α in KMS-11 cells using CRISPR/Cas9 gene editing. In contrast to parental IRE1α wild-type (WT) KMS-11 cells, 3 independent IRE1α knockout (KO) clones showed a complete absence of IRE1α protein and failed to up-regulate XBP1s in response to the ER stressor thapsigargin (Tg) (*SI Appendix*, Fig. S2*A*). Upon s.c. injection into C.B-17 SCID mice, parental IRE1α WT KMS-11 cells formed readily palpable tumors that reached a mean volume of ~500 mm^3 by 29 d; in contrast, all 3 IRE1α KO clones failed to sustain appreciable tumor growth (Fig. 2*A* and *SI Appendix*, Fig. S2*B*). Importantly, reconstitution of IRE1α KO cells with WT IRE1α (WT ^{R}IRE1α) rescued tumor growth, whereas transfection with a kinase-dead D688N mutant (KD ^{R}IRE1α) failed to do so (Fig. 2*B* and *SI Appendix*, Fig. S2 *C* and *D*). Thus, s.c. establishment and growth of KMS-11 MM xenografts in mice requires IRE1α and depends on its kinase function.

To examine the relative importance of XBP1s for MM tumor growth in vivo, we disrupted the XBP1 gene by CRISPR/Cas9 in KMS-11 cells. Similar to the IRE1α KO clones, two independent XBP1 KO clones failed to grow appreciably upon s.c. injection into C.B-17 SCID mice, while parental IRE1α WT cells formed tumors as expected (Fig. 2*C* and *SI Appendix*, Fig. S2*E*). Thus, in vivo growth of KMS-11 tumor xenografts requires the IRE1α–XBP1s pathway.

To ascertain whether IRE1α depletion alone, or its combination with standard anti-MM therapies, affects growth of preestablished tumors, we allowed s.c. implanted KMS-11 or RPMI-8226 cells carrying Dox-inducible shRNAs against IRE1α or nontargeting control (NTC) to form palpable tumors of ~200 mm^3 and then initiated treatment with Dox. While NTC shRNA induction had no impact on tumor growth, IRE1α knockdown substantially suppressed tumor progression, in conjunction with a marked decrease in XBP1s protein levels; this led to 61% tumor-growth inhibition (TGI) in KMS-11 and 70% TGI in RPMI-8226 xenografts (Fig. 2 *D* and *E* and *SI Appendix*, Fig. S2 *F–J*). Furthermore, treatment in the KMS-11 model with the maximum tolerated dose (MTD) of the PI bortezomib led to 54% TGI, while the combination of IRE1α knockdown and bortezomib treatment afforded 91% TGI ($P < 0.05$ compared with IRE1α knockdown alone) (Fig. 2*D* and *SI Appendix*, Fig. S2*G*), indicating strong tumor attenuation. Similarly, treatment in the RPMI-8226 model with the MTD of the IMiD lenalidomide led to 61% TGI, while combination of IRE1α knockdown and lenalidomide administration achieved 110% TGI ($P < 0.01$ compared with IRE1α knockdown alone) (Fig. 2*E* and *SI Appendix*, Fig. S2*H*), indicating tumor regression. Together, these results show that genetic disruption of IRE1α markedly inhibits initiation and progression of MM tumor xenografts and increases sensitivity to established anti-MM agents. Thus, perturbation of IRE1α has significant potential to enhance the efficacy of MM therapy.

To explore mechanistically how disruption of IRE1α inhibits tumor growth, we examined the regulation of genes that encode key ERAD mediators (14, 17). IRE1α or XBP1 KO in KMS-11 cells attenuated in vitro Tg-induced mRNA expression of the E3 ubiquitin ligase SYVN1, the E2 ubiquitin-conjugating enzyme UBE2J1, and factors required for the recognition and extraction of terminally misfolded proteins from the ER, namely EDEM1, DERL2, VIMP, DNAJC10, and ERLEC1 (Fig. 2*F*). Similarly, IRE1α knockdown in RPMI-8226 cells reduced the constitutive mRNA levels of these ERAD machinery genes (Fig. 2*G*). We next examined the secretion of Ig light chains. IRE1α KO via CRISPR/Cas9 or knockdown via anti-IRE1α shRNA, but not anti-NTC shRNA, significantly attenuated secretion of Ig light chains by KMS-11 and RPMI-8226 cells and increased intracellular retention of light chain in the latter cells (Fig. 2 *H* and *I* and *SI Appendix*, Fig. S2 *K–M*). Furthermore, IRE1α depletion in RPMI-8226 cells both in vitro and in vivo inhibited secretion of several cytokines, that is, vascular endothelial growth factor (VEGF), interleukin (IL)-6, IL-10, and IL-1α, as well as the chemokines IL-8 (CXCL8) and interferon-inducible protein (IP)-10 (CXCL10) (Fig. 2*J* and *SI Appendix*, Fig. S2*N*). Interestingly, IRE1 KO did not significantly alter ER morphology in xenografted KMS-11 tumor cells, suggesting that ER ultrastructural organization does not depend on IRE1α in these cells (*SI Appendix*, Fig. S2*O*). The perturbation of both ERAD and protein secretion in MM cells lacking IRE1α may compromise their growth in vivo (23, 40).

Small-Molecule Inhibition of IRE1α Kinase Attenuates Growth of s.c. and Orthometastatic Human MM Xenografts. Next, we investigated whether pharmacologic inhibition of IRE1α could recapitulate the impact of genetic disruption on MM tumor growth. Because XBP1s depletion through direct IRE1α RNase inhibition can lead to hyperphosphorylation of the kinase domain (20, 41), we chose to block IRE1α further upstream, at the kinase level. To test whether IRE1α autophosphorylation controls RNase activation in MM cells, we reconstituted KMS-11 IRE1α KO cells with cDNA expression plasmids encoding WT (WT ^{R}IRE1α) or mutant variants of IRE1α enzymatically deficient in kinase activity (D688N, KD ^{R}IRE1α) or in autophosphorylation on the kinase-activation loop (S724A S726A S729A triple mutant, PD ^{R}IRE1α). Upon ER stress, cells expressing WT IRE1α, but not the KD or PD mutants, displayed increased production of XBP1s at the protein and mRNA levels (Fig. 3*A*). Thus, disruption of either the kinase function or the autophosphorylation sites of IRE1α in MM cells blocks RNase activation and XBP1s production. This finding is consistent with the failure of KD ^{R}IRE1α to rescue in vivo growth of KMS-11 tumor xenografts (Fig. 2*B*).

Harrington et al. (35) identified kinome-selective inhibitors of IRE1α kinase, including compounds **16** and **18** (Fig. 3*B*). We synthesized both molecules and confirmed their binding to a recombinant IRE1α protein comprising the kinase and RNase domains, and their ability to inhibit its RNase activity toward a synthetic XBP1-based RNA substrate, as well as cellular IRE1α activity measured by an XBP1s-luciferase reporter assay (*SI Appendix*, Fig. S3*A*) (11, 24). We compared the kinase selectivity of these compounds by testing 220 kinases via KinomeScan. Compound **18** displayed significantly better selectivity than **16**, with >70% inhibition of only 1 off-target kinase (JNK2), compared with 7 for **16;** another published IRE1α kinase inhibitor called KIRA6 (42) was poorly selective, with >70% attenuation of 64/220 kinases (Fig. 3*B* and *SI Appendix*, Fig. S3 *A* and *B*). Of note, whereas compound **18** significantly attenuated spheroid growth of KMS-11 cells on Matrigel, two different JNK-specific inhibitors, JNK-IN-8 and SP600125, had only minor impact (*SI Appendix*, Fig. S3*C*). Furthermore, mRNA expression of JNK2 in RPMI-8226 and OPM-2 cells was relatively low compared with

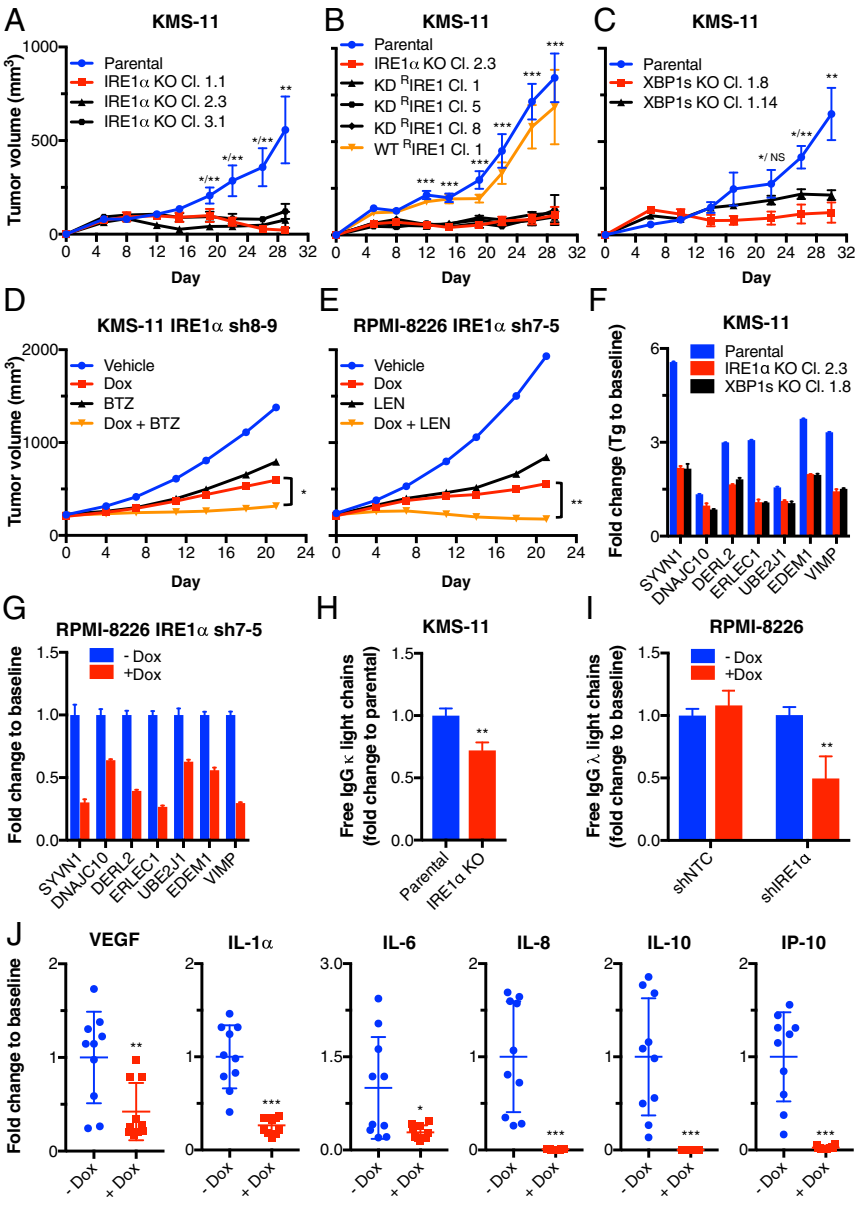


Fig. 2. Genetic disruption of IRE1α or XBP1 attenuates growth of s.c. human MM xenografts in mice. (*A*) IRE1α was disrupted by CRISPR/Cas9 in KMS-11 cells. Parental or corresponding knockout (KO) clones were injected s.c. (SC) into C.B-17 SCID mice and monitored for tumor growth. (*B*) KMS-11 IRE1α KO Cl. 2.3 cells were stably transfected with expression plasmids encoding wild-type (WT) IRE1α (WT ^{R}IRE1α) or kinase-dead (KD) D688N mutant IRE1α (KD ^{R}IRE1α), injected SC into mice and monitored for tumor growth. (*C*) XBP1 was disrupted by CRISPR/Cas9 in KMS-11 cells. Parental or corresponding KO clones were injected SC and monitored for tumor growth (mean tumor volume ± SEM). (*D* and *E*) KMS-11 (*D*) or RPMI-8226 (*E*) cells with Dox-inducible shRNAs against IRE1α were inoculated SC and allowed to establish tumors. Mice were then randomized into treatment groups ($n = 10$ mice per group in *D*, $n = 8$ or 9 mice per group in *E*): vehicle (sucrose), Dox in drinking water (*D* and *E*), bortezomib (BTZ), alone or with Dox (*D*), or lenalidomide (LEN), alone or with Dox (*E*), and tumor growth was monitored. Individual mouse data are in *SI Appendix*, Fig. S2 *G* and *H*. (*F*) KMS-11 parental, IRE1α, or XBP1s KO cells were treated with DMSO or Tg (100 nM) for 6 h and analyzed by RNAseq. Fold change in mRNA is shown for the indicated ERAD components. (*G*) Human free IgG κ light chains were quantified in KMS11 parental or IRE1α KO Cl. 2.3 cell supernatants by ELISA 9 h after seeding. Fold change in secretion for equal cell numbers is shown. (*H*) RPMI-8226 cells with Dox-inducible shRNAs against IRE1α were incubated with Dox (0 or 1 μg/mL) for 3 d and analyzed by RT-qPCR. Fold change in mRNA is shown for the indicated ERAD components. (*I*) RPMI-8226 cells with Dox-inducible shRNAs against NTC or IRE1α were incubated with Dox (0 or 1 μg/mL) for 3 d, equal number of cells seeded, and human free IgG λ light chains quantified in cell supernatants by ELISA 9 h later. (*J*) Mice bearing SC tumor xenografts of RPMI-8226 cells with Dox-inducible shRNAs against IRE1α were treated with Dox in drinking water, and sera were collected and analyzed by luminex for fold change in the concentrations of indicated cytokines and chemokines. $^{*}P < 0.05$, $^{**}P \leq 0.01$, $^{***}P \leq 0.001$. NS, not significant.

most other cell lines in the CCLE dataset (*SI Appendix*, Fig. S3*D*). Therefore, any off-target inhibition of JNK2 by IRE1α kinase inhibitors is unlikely to be functionally significant in these MM cell lines. Quantitative PCR analysis demonstrated that **18** inhibited constitutive IRE1α-mediated XBP1s production in RPMI-8226 cells, as well as Tg-induced XBP1s mRNA generation and RIDD activity toward DGAT2 mRNA in KMS-11 cells, with half-maximal inhibitory concentration of 82.5 and 76.5 nM, respectively (*SI Appendix*, Fig. S3 *E* and *F*).

To gain structural insight into the interaction of compound **18** with its target, we cocrystallized it with purified recombinant IRE1α kinase–RNase protein and determined an X-ray structure

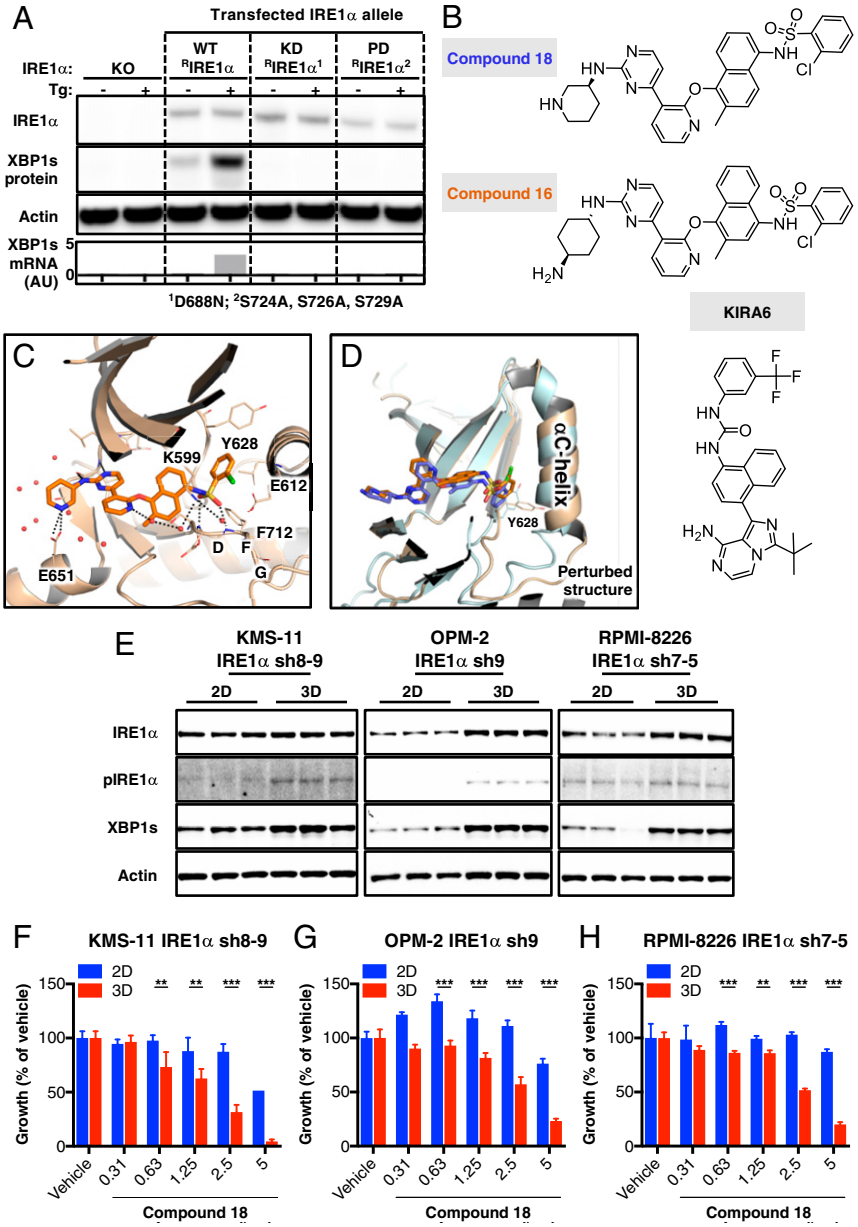


Fig. 3. Importance of IRE1α kinase in RNase activation in growth of MM cell lines in 3D versus 2D. (*A*) KMS-11 IRE1α knockout (KO) cells (Cl. 2.3) were transiently transfected with expression plasmids encoding wild-type IRE1α (WT ^{R}IRE1α), a "kinase-dead" D688N mutant of IRE1α (KD ^{R}IRE1α), or an "autophosphorylation-deficient" S724A, S726A, S729A triple mutant of IRE1α (PD ^{R}IRE1α). Cells were then incubated in the absence or presence of thapsigargin (Tg, 100 nM) for 3 h and analyzed either by IB for levels of the indicated proteins or by RT-qPCR for mRNA levels of XBP1s. (*B*) Chemical structures of compounds **18** and **16** (35) and KIRA6 (42). (*C*) A close-up view of the crystal structure of **18** in complex with the kinase-RNase portion of IRE1α. The protein is rendered in ribbons with key residues in the ligand-binding pocket shown as sticks. Water molecules near the ligand are shown in red spheres. Black dashed lines indicate hydrogen bonding interactions. (*D*) Comparison between the cocrystal structures of **18** (colored in wheat and orange versus **16** (PDB ID code 4U6R, colored cyan and blue) bound to IRE1α. The C-terminal end of the αC-helix displays significant conformational changes between the two structures. (*E*) KMS-11, OPM-2, and RPMI-8226 cells were seeded on standard tissue culture plates (2D) or ULA plates followed by centrifugation to form single spheroids (3D). After 96 h, cells were lysed and analyzed by IB for indicated proteins. (*F–H*) Cells were seeded either in the 2D or 3D setting, treated for 150 h with vehicle (DMSO) or compound **18** at the indicated concentrations, and analyzed for cell growth by cell confluence using an Incucyte instrument (*F*) or cell viability using CellTiter-Glo 3D (*G* and *H*). $^{**}P \leq 0.01$, $^{***}P \leq 0.001$.

at 2.20-Å resolution. Consistent with its ability to act as a kinase inhibitor of IRE1α, **18** binds in the ATP docking site (Fig. 3*C* and *SI Appendix*, Fig. S3*G*). The aminopyrimidine anchors at the hinge and delivers the chloro-phenyl tail moiety to the kinase back pocket. The sulfonamide forms hydrogen bonds with the Asp, Phe, Gly (DFG) backbone in a DFG-in conformation and accepts a hydrogen bond from the catalytic Lys residue, K599. The Lys–Glu salt bridge typically seen in the active state of kinases is absent in this structure, as K599 and E612 are separated by 5.4 Å. The combined effects of back-pocket binding and salt-bridge disruption may induce critical structural changes throughout the cytoplasmic region that ultimately afford allosteric inhibition of the RNase. This ligand-binding mode is reminiscent of the interaction of **16** with IRE1α (Protein Data Bank [PDB] ID code 4U6R) (35). However, the 1,4 substituted naphthyl linker of **18** pulls back from the kinase N-lobe by ∼1.0 Å compared with the

1,5 substituted naphthyl linker of **16**. Further comparison reveals that **18** displaces the C-terminal end of the Cα-helix to a greater extent than does **16**, where residue Y628 shows the most difference in side-chain conformation (Fig. 3*D*). Although we cannot rule out that crystal packing may influence this, structural changes in the Cα-helix may contribute to the improved selectivity of **18** against IRE1α. We therefore chose the latter molecule as a tool for further studies.

We next investigated the effect of compound **18** on MM cells growing on standard tissue culture plates (2D) compared with ULA plates (3D). As a prelude, we examined the activation state of the IRE1α pathway in cells growing in 2D or 3D. IB analysis of KMS-11, OPM-2, and RPMI-8226 cells suggested elevated activity of IRE1α in 3D versus 2D settings, evident by detectable increases in IRE1α protein and/or phosphorylation and in XBP1s levels (Fig. 3*E*). Importantly, whereas both compound **18** and the previously published IRE1α RNase inhibitor 4μ8c (43) markedly inhibited 3D growth of all three cell lines, these inhibitors had much weaker impact on 2D growth (Fig. 3 *F–H* and *SI Appendix*, Fig. S3 *H–N*). We obtained similar results with three additional B-derived, nonmyeloma cancer cell lines that expressed detectable baseline levels of IRE1α and XBP1s (*SI Appendix*, Fig. S3 *O–R*), supporting the importance of IRE1α for 3D growth of such cells.

Next, we turned to investigate the effect of compound **18** on growth of MM tumor xenografts in vivo. Upon intraperitoneal (IP) injection at 30 mg/kg, once (QD) or twice (BID) per day, in C.B-17 SCID mice, **18** achieved initial plasma concentrations of 4.3 μM and remained above 0.1 μM for ∼8 h (*SI Appendix*, Fig. S4*A*). These data suggested potentially sufficient exposure to this compound to attain significant, though perhaps incomplete, IRE1α inhibition in vivo. Comparable to the effect of IRE1α shRNA depletion, BID treatment of mice bearing preestablished KMS-11 tumor xenografts with **18** led to a substantial reduction in XBP1s protein, in conjunction with 51% TGI (Fig. 4*A* and *SI Appendix*, Fig. S4 *B* and *C*). We next tested the effect of QD administration of the compound on growth of OPM-2 tumor xenografts; we observed 70% TGI, comparable to Dox-induced shRNA-mediated knockdown of IRE1α (Fig. 4*B* and *SI Appendix*, Fig. S4 *D* and *E*). Thus, pharmacologic IRE1α kinase inhibition recapitulated the impact of shRNA-based IRE1α depletion on growth of MM xenografts.

We then turned to a more stringent orthometastatic model of MM, in which luciferase and mCherry double-labeled RPMI-8226 cells, injected into the tail vein of NSG mice, develop widespread malignant disease with bone marrow involvement over a period of 6 wk (*SI Appendix*, Fig. S4*F*) (44). Treatment of mice bearing established malignant disease with **18** over two subsequent weeks led to a marked reduction in tumor burden, evident by diminished luminescence (Fig. 4*C*): Whereas 3/3 control mice displayed tumor progression over baseline, only 1/5 **18**-treated mice showed tumor progression, while another 1/5 exhibited tumor stasis, and 3/5 showed substantial tumor regression. Thus, pharmacologic inhibition of IRE1α kinase in vivo disrupts growth of MM xenografts not only in the s.c. setting but also in the more clinically relevant orthometastatic bone marrow microenvironment.

IRE1α Kinase Inhibition Reduces Viability of Patient-Derived MM Cells While Sparing Normal Cells. Cancer cell lines may acquire further genetic or epigenetic alterations upon prolonged passage that could diverge them from their primary source. Therefore, to gain a more direct appraisal of the importance of IRE1α for primary MM cell survival, we tested the effect of compound **18** on viability of $CD138^+$ plasma cells from the donated bone marrow or peripheral blood of MM patients clinically treated in the United States or the European Union (*SI Appendix*, Fig. S5*A*). Incubation with **18** led to marked reductions in viability of the malignant $CD138^+$ MM cells, but not the associated nonmalignant

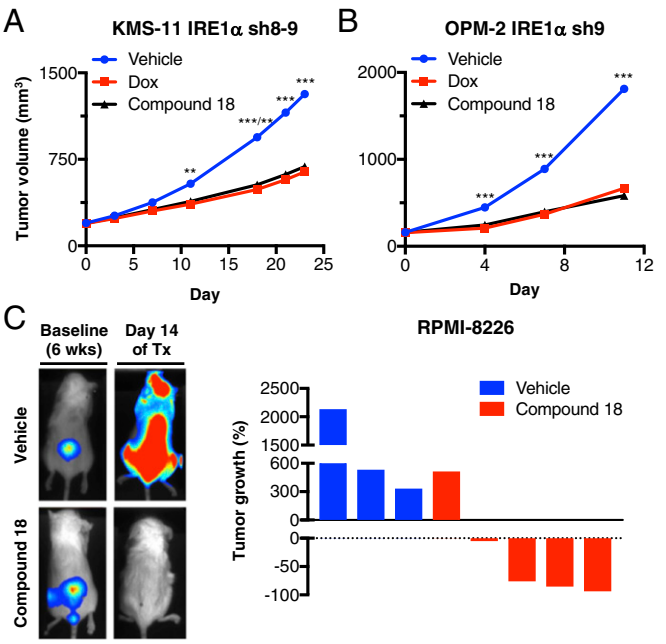


Fig. 4. Small-molecule inhibition of IRE1α kinase attenuates s.c. and orthometastatic growth of human MM xenografts in mice. (*A*) KMS-11 cells stably transfected with doxycycline (Dox)-inducible shRNAs against IRE1α were inoculated s.c. into C.B-17 SCID mice and allowed to establish tumors of ∼200 mm^3. Mice were then randomized into the following groups (n = 15 per group): vehicle, Dox in the drinking water (0.5 mg/kg), or compound **18** (30 mg/kg) intraperitoneally (IP) twice per day (BID). Tumor growth was monitored over 24 d. Individual tumor data are shown in *SI Appendix*, Fig. S4*C*. (*B*) OPM-2 cells stably transfected with Dox-inducible shRNAs against IRE1α were inoculated s.c. into C.B-17 SCID mice and allowed to establish tumors of ∼160 mm^3. Mice were then randomized (n = 14 per group) treated as in *A* with either vehicle, Dox in the drinking water, or compound **18** IP once per day and monitored for tumor growth over 11 d. Individual tumor data are shown in *SI Appendix*, Fig. S4*E*. (*C*) RPMI-8226 cells expressing plasmids encoding mCherry and luciferase were injected i.v. via the tail vein of nonirradiated NOD/SCID/IL2r$\gamma^{-/-}$ mice and tumors were allowed to establish in the bone marrow over a period of 6 wk. Tumor burden was monitored by in-life imaging of luminescence. After 6 wk, mice were grouped out based on similar tumor burden, treated with vehicle (n = 3) or compound **18** (30 mg/kg IP, BID, n = 5) for 2 wk, and analyzed for tumor burden. One control mouse died during anesthesia and one treated mouse was killed due to weight loss. Luminescence images of representative mice are depicted on the left. The tumor burden of each mouse is shown as percent tumor growth on day 14 (at the end of 8 wk) compared with day 0 of treatment (Tx, at the end of 6 wk). $^{**}P \leq 0.01$, $^{***}P \leq 0.001$.

$CD138^-$ cells, in the majority of cases (Fig. 5 *A* and *B*). In both MM cohorts, samples from newly diagnosed patients as well as subjects whose disease relapsed after 1 to 4 prior lines of therapy showed dose-dependent sensitivity to **18** (Fig. 5 *C* and *D*). Comparison of the impact of **18** and 4μ8c on an additional MM bone marrow aspirate suggested greater loss of plasma-cell viability with the former (*SI Appendix*, Fig. S5 *B* and *C*). Importantly, exposure to **18** did not reduce viability of $CD138^+$ cells from three nonmalignant bone marrow aspirates (Fig. 5*E*). Thus, IRE1α kinase inhibition can selectively disrupt survival of primary malignant MM cells while sparing nonmalignant hematopoietic cells, including plasma cells. The impact on both naïve and posttreatment-relapsed MM samples suggests that IRE1α inhibition has the potential to provide clinical benefit across several different lines of therapy.

We next turned to investigate whether pharmacologic IRE1α kinase inhibition disrupts normal function of other cell types. Inducible gene-knockout studies in mice have suggested that the

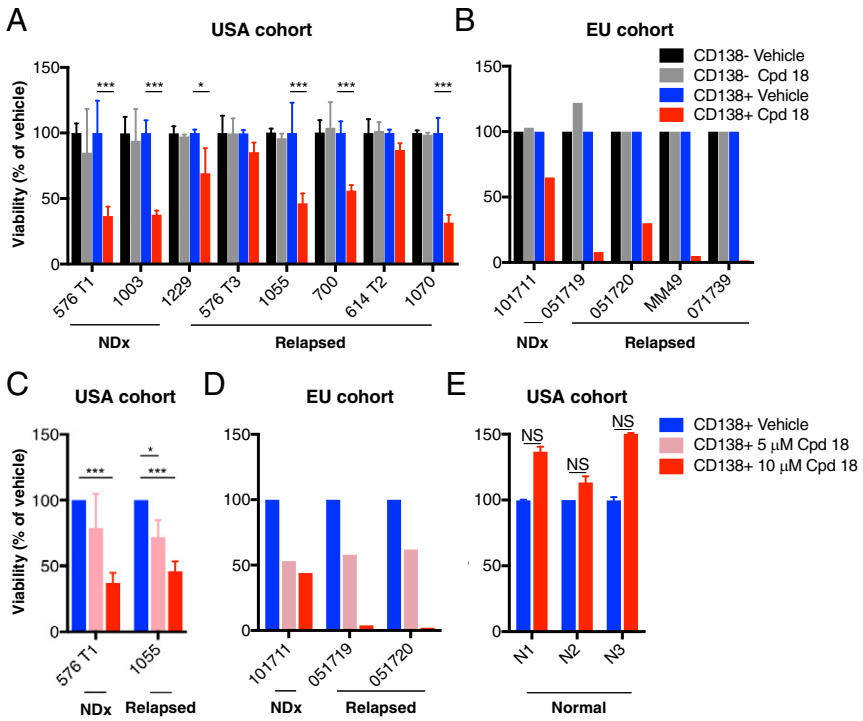


Fig. 5. Small-molecule inhibition of IRE1α kinase reduces viability of CD138$^+$ MM cells in patient-derived samples without disrupting CD138$^-$ cells. (*A–E*) Bone marrow aspirates or peripheral blood obtained in the United States (*A*, *C*, and *E*) or European Union (*B* and *D*) from patients with newly diagnosed (NDx) or relapsed MM. Further information about age, gender, disease state, cytogenetics, and prior treatments is included in *SI Appendix*, Fig. S5*A*. Samples were cultured for 48 (*A–C* and *E*) or 72 h (*D*) with either vehicle (DMSO) or 10 μM compound (Cpd) **18** (*A*, *B*, and *E*), or two dose levels, 1 and 10 μM of compound (Cpd) **18** (*C* and *D*). Samples were then analyzed for viability by flow cytometry, with gating on CD138$^+$ or CD138$^-$ cells. Nonmalignant bone marrow aspirates ($n = 3$) were similarly tested and are depicted for comparison (*E*). Data represent mean ± SD of triplicate determinations except where triplicates were not possible due to insufficient sample size. NS, not significant. *$P < 0.05$, ***$P \leq 0.001$.

IRE1α–XBP1s pathway may support insulin secretion by pancreatic cells (45, 46) and homeostasis of hepatocytes (47). Therefore, we first verified the ability of compound **18** to inhibit XBP1s induction in human pancreatic islet 3D microtissues, which contain all of the endocrine cell types and can retain viability and function in culture for up to 4 wk (48). At 2.4 μM, **18** suppressed Tg-induced XBP1s production to baseline levels (Fig. 6*A*), confirming effective IRE1α pathway inhibition. Importantly, **18** did not decrease viability, nor did it perturb glucose-stimulated insulin secretion even at higher concentrations up to 7.5 μM (Fig. 6 *B* and *C*). We obtained similar results with rat pancreatic microislets (*SI Appendix*, Fig. S6 *A* and *B*). Furthermore, despite completely blocking tunicamycin-induced XBP1s expression by primary human hepatocytes at 3 μM, treatment with **18** did not impact hepatocyte viability at concentrations up to 6 μM (Fig. 6 *D* and *E*). In addition to these in vitro experiments, we performed a tolerability study of compound **18** in C.B-17 SCID mice by IP injection at 10, 30, or 100 mg/kg BID over 7 d. Whereas some mice did not tolerate the 100 mg/kg dose, animals administered up to 30 mg/kg completed the dosing period with only a minor weight loss compared with vehicle-treated controls, along with minimal changes in serum albumin and in the bone marrow myeloid compartment. Some peritoneal inflammation was seen in both vehicle- and **18**-treated mice, likely due to the repeated IP injections. There were no other compound-related changes in hematology, serum chemistry, or organ weights; furthermore, there were no gross or microscopic pathology findings overall, notably including in secretory organs such as the pancreas and salivary glands (*SI Appendix*, Fig. S6 *C* and *D*). In a separate study, dosing of **18** at 30 mg/kg QD for 3 wk did not cause significant alterations in hepatic, renal, and pancreatic endocrine functional markers in serum (*SI Appendix*, Fig. S6*E*). Together, these results suggest that IRE1α kinase inhibition can achieve effective MM tumor disruption without overt negative effects on normal tissue homeostasis.

Discussion

MM cells may co-opt the IRE1α–XBP1s pathway to mitigate persistent ER stress, caused by Ig production and a nutrient/oxygen-poor bone marrow microenvironment (27). However, recent studies have raised significant doubt concerning the validity of IRE1α as a potential MM therapeutic target: Lowered levels of XBP1s correlated with PI resistance in MM cells (49), and IRE1α kinase inhibition blocked XBP1s yet did not affect MM cell viability in 2D culture (35, 49). Although work based on salicylaldehyde small-molecule RNase inhibitors supported a protumorigenic role of IRE1α in MM (31, 32), such compounds are highly protein-reactive, and their selectivity versus off targets is difficult to confirm (36). Direct loss-of-function studies specifically addressing the importance of the kinase module of IRE1α for MM growth in vivo have been lacking.

To interrogate the requirement of IRE1α for MM growth, we employed a series of strategies to disrupt it at the gene, transcript, or kinase level, in diverse model systems. Our in vitro studies showed that IRE1α depletion by shRNAs markedly attenuates growth of several MM cell lines in 3D spheroid settings—a scenario that was not previously investigated in connection with IRE1α. Consistent with this elevated dependency, MM cells growing in 3D showed increased baseline activity of the IRE1α pathway compared with 2D. In vivo, both IRE1α KO and XBP1s KO in KMS-11 MM cells profoundly disrupted their ability to form s.c. tumor xenografts in mice. Critically, reconstitution of WT but not kinase-dead IRE1α into KO cells rescued tumor growth, validating the conclusion that disrupted growth was specifically due to IRE1α kinase loss of function. These findings demonstrate a crucial requirement of the

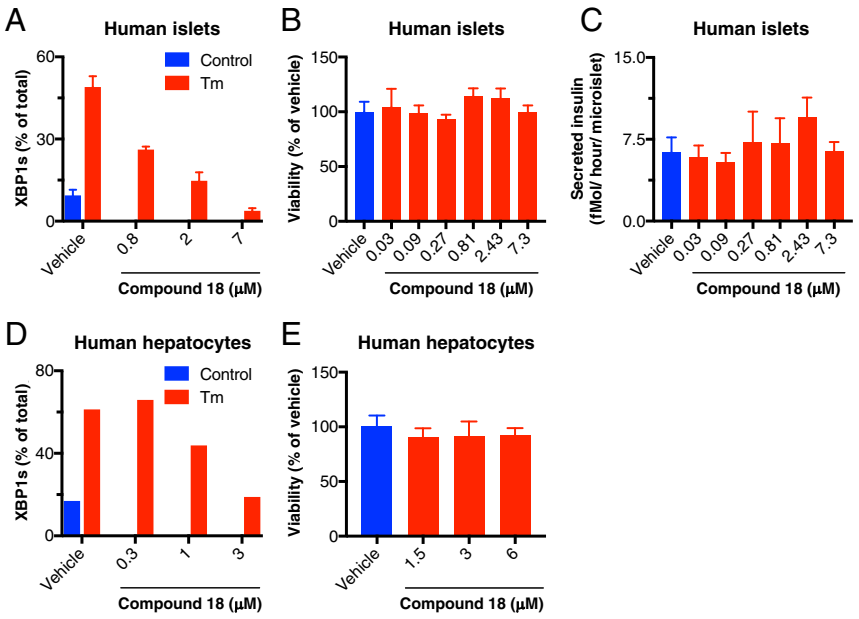


Fig. 6. IRE1α kinase inhibition preserves survival and insulin secretion by pancreatic islet 3D microtissues and viability of primary hepatocytes. (*A*–*C*) Human pancreatic islets were isolated, dissociated, replated in microtiter wells (1,000 cells per drop), and allowed to form 3D microtissues over 7 d. Microtissues (n = 5 per treatment) were then (*A*) treated for 24 h with either vehicle control (DMSO) or tunicamycin (Tm, 5 μg/mL) in addition to either vehicle (DMSO) or compound **18**, lysed, and then analyzed for XBP1s mRNA levels by RT-qPCR (%XBP1s mRNA is the ratio of XBP1s mRNA/(XBP1s mRNA+XBP1u mRNA); or (*B* and *C*) incubated for 7 d in the presence of either vehicle (DMSO) or compound **18** and then (*B*) analyzed for cell viability by CellTiter-Glo; or (*C*) challenged with glucose (16.7 mM) for 1 h and analyzed for insulin secretion by ELISA. (*D* and *E*) Human primary hepatocytes were treated for 8 h with either control or Tm in addition to either vehicle or compound **18** and analyzed for XBP1s levels as above by RT-qPCR (*D*). Alternatively, hepatocytes were cultured for 48 h in the presence of vehicle (DMSO) or compound **18** and analyzed for cell viability by CellTiter-Glo (*E*).

IRE1α pathway for in vivo MM growth, while other, kinase- or XBP1s-independent functions of IRE1α such as RIDD or JNK activation may be less important in the context of MM. IRE1α depletion by shRNAs clearly inhibited the growth of preformed s.c. KMS-11 and RPMI-8226 tumor xenografts, implicating IRE1α not only in promoting tumor initiation but also progression. Remarkably, the extent of TGI was directly comparable between IRE1α knockdown and the established frontline MM therapy agents bortezomib or lenalidomide. Furthermore, combination of IRE1α depletion with bortezomib or lenalidomide significantly increased the extent of TGI compared with respective monotherapies. Mechanistically, IRE1α knockdown decreased mRNA expression of multiple ERAD components known to be induced by XBP1s. Moreover, it diminished the ability of MM cells to secrete Ig light chains as well as several cytokines and chemokines, some of which have previously been shown to support malignant plasma cell growth in vitro and in vivo (1, 23, 33, 40). In contrast, IRE1α disruption did not significantly alter ER morphology. Together, these results suggest that IRE1α inhibition has potential to provide significant clinical benefit, either alone or in combination with other MM therapies known to disrupt protein homeostasis (33, 50).

To further examine the requirement for IRE1α's kinase moiety, we first confirmed its importance for RNase activation by mutational perturbation of the kinase catalytic core or its target autophosphorylation sites. We then evaluated three compounds that bind to IRE1α's ATP docking site and exert allosteric inhibition of RNase activation (35, 42). One of these, compound **18**, displayed an improved ability to displace the Cα helix in the kinase domain and excellent selectivity toward IRE1α versus 220 other kinases. In keeping with the results of genetic IRE1α disruption, **18** inhibited growth of MM cells in 3D settings more substantially than in 2D. The IRE1α RNase inhibitor 4μ8c similarly attenuated 3D growth of MM cells, confirming the involvement of IRE1α. In mice, **18** displayed sufficient exposure upon IP administration to enable marked inhibition of XBP1s production in tumors. In concert, **18** significantly attenuated s.c. growth of KMS-11 and OPM-2 xenografts. Thus, pharmacologic inhibition of IRE1α via its kinase moiety recapitulated the impact of genetic IRE1α disruption on MM tumor growth.

To address the importance of IRE1α in a more clinically relevant MM microenvironment, we implemented an orthometastatic model, in which malignant MM cells injected intravenously (i.v.) home to the bone marrow to disseminate malignant disease. Treatment with **18** in this setting led to tumor stasis or regression in most of the animals, compared with aggressive tumor progression in the vehicle-treated controls. Thus, MM cells require IRE1α kinase function in vivo to sustain advanced malignant growth in the bone marrow.

Establishing the excellent kinase selectivity of compound **18** afforded a unique opportunity to examine more reliably the impact of specific IRE1α inhibition on patient-derived MM cells. Remarkably, the compound caused a substantial reduction in viability of malignant $CD138^+$ cells in the majority of MM patient samples, including newly diagnosed tumors as well as tumors that relapsed after 1 or more lines of prior therapy with clinically established agents. In contrast, to its effect on malignant plasma cells, **18** did not significantly reduce viability of accompanying nonmalignant cells in the same MM samples; it also spared both $CD138^+$ plasma cells and $CD138^-$ cells in nonmalignant bone marrow aspirates. Treatment with the IRE1α RNase inhibitor 4μ8c also reduced viability of MM patient-derived $CD138^+$ plasma cells, further confirming the reliance of these cells on IRE1α. In preclinical safety experiments, while **18** achieved complete XBP1s suppression in pancreatic microislets, it disrupted neither viability nor the capacity of these tissues to secrete insulin in response to glucose challenge. Similarly, **18** did not impact viability of primary human hepatocytes in vitro. In mice, at doses that effectively inhibited tumor growth, **18** did not significantly alter normal homeostasis of numerous tissues and organ systems examined, including secretory cells. Taken together, these results suggest that

malignant MM cells harbor an enhanced dependency on the IRE1α–XBP1s pathway compared with nonmalignant cell types, highlighting this pathway as a unique vulnerability that could be clinically exploited to treat MM across multiple stages. Nevertheless, future testing of IRE1α inhibitors in human clinical trials will necessitate the development of orally available compounds and more comprehensive safety studies in suitable model organisms. In addition, it would be interesting to investigate the effect of such inhibitors on MM tumor growth in immunocompetent mice, in light of recent evidence that disruption of XBP1s augments antitumor immunity in syngeneic models of epithelial cancer (6).

In conclusion, our work provides definitive preclinical evidence validating IRE1α as a potential therapeutic target for MM. IRE1α may play an important role in augmenting malignant growth of MM cells by enabling their adaptation to chronic ER stress through elevated ERAD capacity. IRE1α may also support the secretion of Ig light chains as well as cytokines and chemokines that enable survival and growth of malignant MM cells in their metabolically restrictive bone marrow microenvironment. Finally, while RNase inhibition of IRE1α also holds promise, our findings provide proof of concept that the kinase domain of IRE1α is likely to provide an effective and safe lever for small-molecule inhibition of this unique dual-function enzyme. This work therefore establishes a compelling rationale to develop clinical-grade kinase-based inhibitors of IRE1α for MM therapy.

Materials and Methods

Detailed methods are provided in *SI Appendix*.

Cell Culture and Experimental Reagents. KMS-11, RPMI-8226, OPM-2, NCI-H929, KMS-27, MOLP-8, LP-1, U266B1, UTMC-2, KMM-1, KMS28-PE, MOLP-2, NU-DUL-1, OCI-LY18, and NALM-6 cells were obtained from ATCC, JCRB, or DSMZ, authenticated by short tandem repeat profiles, and tested to ensure they were mycoplasma-free within 3 mo of use. All cell lines were cultured in RPMI1640 media supplemented with 10% (vol/vol) FBS (Sigma), 2 mM glutaMAX (Gibco), and 100 U/mL penicillin plus 100 μg/mL streptomycin (Gibco).

Thapsigargin (Sigma) was used at a concentration of 100 nM and tunicamycin (Sigma) at 5 μg/mL. Doxycycline was from Clontech. Compound 16/**16**, compound 18/**18** (35), 4μ8c (43), JNK-IN-8, and SP600125 (Sigma) were dissolved in DMSO for cellular experiments and used at the indicated concentrations. Antibodies (Abs) for IRE1α (3294), β-actin (3700), and GAPDH (5174) were from Cell Signaling Technology. Ab for detection of human IgG light chains (709-005-149) was from Jackson ImmunoResearch. Abs for XBP1s and pIRE1 (21) were generated at Genentech. Secondary antibody (711-035-152) was from The Jackson Laboratory.

Two-Dimensional Proliferation Assays. For compound **18** and 4μ8c serial dilution studies, RPMI-8226 IRE1α sh7-5 and OPM-2 IRE1α sh9, NU-DUL-1, OCI-LY18, and NALM-6 cells were plated in flat clear-bottom 96-well plates (Corning) at 2.5×10^3 cells per well; KMS-11 IRE1α sh8-9 cells were seeded in standard 6-well plates (Corning) at 1×10^5 cells per well. Compound **18** and 4μ8c were used at the indicated concentrations. After 150 h, cell viability of RPMI-8226 IRE1α sh7-5 and OPM-2 IRE1α sh9, NU-DUL-1, OCI-LY18, and NALM-6 cells was assessed using an ATP-consumption assay (CellTiter-Glo 3D; Promega) and measured in a luminescence reader (Envision; PerkinElmer). Cell confluency of KMS-11 IRE1α sh8-9 cells was measured using a real-time imaging system (IncuCyte; Essen Bioscience). Frames were captured at 4-h intervals using a 10× objective. Assays were run at least in triplicates.

Three-Dimensional Spheroid Proliferation Assays. For IRE1α knockdown experiments, KMS-11 IRE1α sh8-9-mCherry, RPMI-8226 IRE1α sh7-5-mCherry, and OPM-2 IRE1α sh9-mCherry cells were pretreated with 0.5 μg/mL Dox for 3 d before plating 1×10^3 cells per well in ULA 96-well plates (Corning). For compound **18** and 4μ8c serial dilution studies in this setting, KMS-11α IRE1 sh8-9, RPMI-8226 IRE1α sh7-5 and OPM-2 IRE1α sh9, NU-DUL-1, OCI-LY18, and NALM-6 cells cells (2.5×10^3 cells per well) were plated in ULA 96-well plates. Compound **18** and 4μ8c were used at the indicated concentrations. Single spheroids were formed by centrifugation (1,000 rpm) for 10 min according to the manufacturer's protocol. Spheroids were imaged using an IncuCyte instrument. Frames were captured at 4-h intervals using a 4× objective and red fluorescence or cell confluence was detected. After 150 h, cell viability of was assessed using CellTiter-Glo 3D.

For Matrigel assays, KMS-11 WT or IRE1α sh8-9 cells were pretreated with 0.5 μg/mL Dox for 3 d before plating 1 to 5×10^3 cells per well on 50 μL/well of Matrigel (Corning) into 96-well plates according to the manufacturer's protocol. To test the impact of JNK inhibition compared with compound **18** in this setting, cells were seeded on Matrigel as described and then treated with serial dilutions of **18**, JNK-IN-8, or SP600125 as indicated. Multispheroids were imaged using an IncuCyte S3 instrument (Essen Bioscience). Frames were captured at 4-h intervals using a 10× objective and cell confluency was detected, and then 150-h cell viability assessed using CellTiter-Glo 3D. Cultures were maintained at 37 °C throughout and run at least in triplicates. Values well were pooled and averaged across all replicates.

Human MM Samples. The effect of compound **18** on viability of MM or normal cells was measured after treatment in ex vivo culture of bone marrow aspirates or blood samples from MM patients or from normal bone marrow donors. All samples were deidentified before use in this study. For cell death assays, mononuclear cells obtained after separation on Ficoll density gradient were cultured in RPMI1640 media supplemented with 5% FCS and 3 ng/mL IL-6, with the indicated concentrations of compound **18** or vehicle control (DMSO) for 48 to 72 h. MM cells were then identified using CD138-PE staining and cell death was assessed by the loss of CD138 staining as previously described (51). MM or normal plasma cells were identified as $CD19^-$, $CD45^-$/dim, $CD38^+$, $CD138^+$, and $CD46^+$.

Pancreatic Islet 3D Microtissue Assays. Human and rodent 3D InSight pancreatic islet microtissues (InSphero AG) were generated from reconstituted dispersed human or rat pancreatic islet cells in a modified manner as described previously (48) retaining the composition of α, β, and δ cells representative of normal endocrine pancreatic islets. Cells were plated in microtiter wells (1,000 cells per drop) and allowed to form 3D microtissues of ∼120 μm in diameter over 7 d ($n = 5$ per treatment). Microtissues were incubated for 7 d with serial dilutions of compound **18** or vehicle control (DMSO) and then viability analyzed by CellTiter-Glo or insulin secretion analyzed after glucose challenge (16.7 mM) for 1 h by ELISA.

Human Hepatocyte Experiments. Normal primary human hepatocytes (Millipore Sigma) were cultured on collagen-coated 96-well plates and assays were performed in serum-free hepatocyte incubation media. Hepatocytes were treated with Tm (5 μg/mL) for 8 h in the presence of compound **18** or vehicle control (DMSO) at the indicated concentration and analyzed for XBP1s levels by RT-qPCR or cultured for 48 h in the presence of vehicle (DMSO) or **18** at the indicated concentrations and analyzed for viability by CellTiter-Glo.

s.c. Xenograft Growth and Efficacy Studies. All procedures were approved by and conformed to the guidelines and principles set by the Institutional Animal Care and Use Committee of Genentech and were carried out in an Association for the Assessment and Accreditation of Laboratory Animal Care-accredited facility.

For tumor growth studies, 10×10^6 KMS-11 parental, IRE1α KO or XBP1 KO clones, or IRE1α KO +WT ^{R}IRE1α or +KD ^{R}IRE1α clones were suspended in HBSS, admixed with 50% Matrigel to a final volume of 100 μL, and injected s.c. in the right flank of 6- to 8-wk-old female C.B-17 SCID mice.

For efficacy studies, 10×10^6 KMS-11 NTC shRNA or IRE1α sh8-9, RPMI-8226 NTC shRNA or IRE1α sh5-7, or OPM-2 IRE1α sh9 cells were prepared and s.c. inoculated as outlined above. Tumors were monitored until they reached a mean tumor volume of ∼150 to 300 mm^3. For efficacy studies of IRE1 shRNA knockdown, animals were randomized into the following treatment groups: 1) 5% sucrose water (provided in drinking water, changed weekly) or 2) Dox (0.5 mg/mL, dissolved in 5% sucrose water, changed 3 times per week). For efficacy studies of IRE1 shRNAs-mediated knockdown in combination with standard of care agents, bortezomib (Velcade; Millennium Pharmaceuticals) or lenalidomide (Revlimid; Celgene Corp.), mice were randomized into one of the following treatment groups: 1) vehicle (5% sucrose water); 2) Dox; 3) bortezomib (0.75 mg/kg, 100 μL total, i.v., twice per week) or lenalidomide (50 mg/kg, 100 μL total, IP, QD for five consecutive days), respectively; or 4) combination of Dox plus bortezomib, or doxycycline plus lenalidomide, respectively.

For compound **18** efficacy studies, animals were randomized into one of the following treatment groups: 1) vehicle controls (35% PEG400 and 10% EtOH in water, 100 μL total, IP, QD) and 5% sucrose water; 2) Dox; or 3) compound **18** (30 mg/kg, 100 μL total, IP, QD or BID as indicated in figure legends).

Orthometastatic Xenograft Efficacy Studies. For the orthometastatic xenograft model, 1×10^6 RPMI-8226-mCherry-Luc cells were injected i.v. via the tail vein of nonirradiated 8-wk-old female NOD/SCID/IL2r$\gamma^{-/-}$ mice (NSG; The Jackson Laboratory). The animals were imaged weekly under isoflurane anesthesia 5 min after i.p. luciferin injection with 200 μL of 25 mg·mL^{-1} D-luciferin (Invitrogen) and imaged on a Photon Imager (BioSpace Laboratory). During image acquisition, animals continued to receive anesthesia from a nose-cone delivery system, while their body temperatures were maintained on a thermostatically controlled platform. Photon counts per min per square centimeter of observational area were calculated and compared using M3 Vision software (BioSpace Laboratory). After 6 wk mice were grouped out into the following treatment groups: 1) vehicle control (100 μL total, IP, BID) or 2) compound **18** (30 mg/kg, 100 μL total, IP, BID). After 14 d, mice were killed by cervical dislocation and bones harvested for fluorescence imaging using a Kodak In-Vivo FX system (Carestream Health Molecular Imaging) and Carestream Molecular Imaging (MI) Software. Excitation and emission wavelengths were fixed at 550 nm and 600 nm, respectively. Fluorescence images were coregistered with X-ray images using the open-source software Image J (https://imagej.nih.gov/ij/).

Statistics. All values are represented as arithmetic mean ± SD if not otherwise indicated in the figure legends. Statistical analysis of the results was performed by unpaired, two-tailed *t* test or ANOVA followed by an appropriate post hoc analysis, including Bonferroni correction to compensate for multiple comparisons. A P value <0.05 was considered significant. All statistical analyses were performed using GraphPad Prism 6 (GraphPad Software, Inc.). For further information regarding statistical analysis, see the section regarding xenograft studies above.

ACKNOWLEDGMENTS. This work was supported in part by an Irvington Postdoctoral Fellowship of the Cancer Research Institute to D.A.A. and by a Howard Hughes Collaborative Innovation Award to P.W. P.W. is an Investigator of the Howard Hughes Medical Institute. We thank Rena Wang and Xiangnan Du for help with cell line generation; Brian Rabinovich for mCherry lentiviral construct design; Jing Peng for help with mouse xenograft studies; Christophe Langouët-Astrie and Shelby Bearrows for technical assistance analyzing primary myeloma samples; members of the A.A. and P.W. laboratories; and Marc Shuman, Stephen Gould, Matthew Wright, Shiva Malek, Daniel Sutherlin, Jessica Sims, Wendy Young, and Ira Mellman for helpful discussions.

1. W. M. Kuehl, P. L. Bergsagel, Multiple myeloma: Evolving genetic events and host interactions. *Nat. Rev. Cancer* **2**, 175–187 (2002).
2. R. L. Siegel, K. D. Miller, A. Jemal, Cancer statistics, 2015. *CA Cancer J. Clin.* **65**, 5–29 (2015).
3. P. Walter, D. Ron, The unfolded protein response: From stress pathway to homeostatic regulation. *Science* **334**, 1081–1086 (2011).
4. C. Hetz, The unfolded protein response: Controlling cell fate decisions under ER stress and beyond. *Nat. Rev. Mol. Cell Biol.* **13**, 89–102 (2012).
5. M. Wang, R. J. Kaufman, Protein misfolding in the endoplasmic reticulum as a conduit to human disease. *Nature* **529**, 326–335 (2016).
6. J. R. Cubillos-Ruiz, S. E. Bettigole, L. H. Glimcher, Tumorigenic and immunosuppressive effects of endoplasmic reticulum stress in cancer. *Cell* **168**, 692–706 (2017).
7. I. Tabas, D. Ron, Integrating the mechanisms of apoptosis induced by endoplasmic reticulum stress. *Nat. Cell Biol.* **13**, 184–190 (2011).
8. J. S. Cox, C. E. Shamu, P. Walter, Transcriptional induction of genes encoding endoplasmic reticulum resident proteins requires a transmembrane protein kinase. *Cell* **73**, 1197–1206 (1993).
9. K. P. Lee *et al*., Structure of the dual enzyme Ire1 reveals the basis for catalysis and regulation in nonconventional RNA splicing. *Cell* **132**, 89–100 (2008).
10. W. Tirasophon, A. A. Welihinda, R. J. Kaufman, A stress response pathway from the endoplasmic reticulum to the nucleus requires a novel bifunctional protein kinase/endoribonuclease (Ire1p) in mammalian cells. *Genes Dev.* **12**, 1812–1824 (1998).
11. A. V. Korennykh *et al*., The unfolded protein response signals through high-order assembly of Ire1. *Nature* **457**, 687–693 (2009).
12. D. Han *et al*., IRE1alpha kinase activation modes control alternate endoribonuclease outputs to determine divergent cell fates. *Cell* **138**, 562–575 (2009).
13. Y. Lu, F. X. Liang, X. Wang, A synthetic biology approach identifies the mammalian UPR RNA ligase RtcB. *Mol. Cell* **55**, 758–770 (2014).
14. K. J. Travers *et al*., Functional and genomic analyses reveal an essential coordination between the unfolded protein response and ER-associated degradation. *Cell* **101**, 249–258 (2000).
15. A. L. Shaffer *et al*., XBP1, downstream of Blimp-1, expands the secretory apparatus and other organelles, and increases protein synthesis in plasma cell differentiation. *Immunity* **21**, 81–93 (2004).
16. D. Acosta-Alvear *et al*., XBP1 controls diverse cell type- and condition-specific transcriptional regulatory networks. *Mol. Cell* **27**, 53–66 (2007).
17. J. L. Brodsky, Cleaning up: ER-associated degradation to the rescue. *Cell* **151**, 1163–1167 (2012).
18. J. Hollien, J. S. Weissman, Decay of endoplasmic reticulum-localized mRNAs during the unfolded protein response. *Science* **313**, 104–107 (2006).
19. J. Hollien *et al*., Regulated Ire1-dependent decay of messenger RNAs in mammalian cells. *J. Cell Biol.* **186**, 323–331 (2009).
20. M. Lu *et al*., Opposing unfolded-protein-response signals converge on death receptor 5 to control apoptosis. *Science* **345**, 98–101 (2014).
21. T. K. Chang, *et al*., Coordination between two branches of the unfolded protein response determines apoptotic cell fate. *Mol. Cell* **71**, 629–636.e5 (2018).
22. A. M. Reimold *et al*., Plasma cell differentiation requires the transcription factor XBP-1. *Nature* **412**, 300–307 (2001).
23. N. N. Iwakoshi *et al*., Plasma cell differentiation and the unfolded protein response intersect at the transcription factor XBP-1. *Nat. Immunol.* **4**, 321–329 (2003).
24. K. Zhang *et al*., The unfolded protein response sensor IRE1alpha is required at 2 distinct steps in B cell lymphopoiesis. *J. Clin. Invest.* **115**, 268–281 (2005).
25. D. Hanahan, R. A. Weinberg, Hallmarks of cancer: The next generation. *Cell* **144**, 646–674 (2011).
26. L. Vincenz, R. Jäger, M. O'Dwyer, A. Samali, Endoplasmic reticulum stress and the unfolded protein response: Targeting the achilles heel of multiple myeloma. *Mol. Cancer Ther.* **12**, 831–843 (2013).
27. M. Wang, R. J. Kaufman, The impact of the endoplasmic reticulum protein-folding environment on cancer development. *Nat. Rev. Cancer* **14**, 581–597 (2014).
28. D. Jiang, M. Niwa, A. C. Koong, Targeting the IRE1α-XBP1 branch of the unfolded protein response in human diseases. *Semin. Cancer Biol.* **33**, 48–56 (2015).
29. D. R. Carrasco *et al*., The differentiation and stress response factor XBP-1 drives multiple myeloma pathogenesis. *Cancer Cell* **11**, 349–360 (2007).
30. T. Bagratuni *et al*., XBP1s levels are implicated in the biology and outcome of myeloma mediating different clinical outcomes to thalidomide-based treatments. *Blood* **116**, 250–253 (2010).
31. I. Papandreou *et al*., Identification of an Ire1alpha endonuclease specific inhibitor with cytotoxic activity against human multiple myeloma. *Blood* **117**, 1311–1314 (2011).
32. N. Mimura *et al*., Blockade of XBP1 splicing by inhibition of IRE1α is a promising therapeutic option in multiple myeloma. *Blood* **119**, 5772–5781 (2012).
33. S. K. Kumar *et al*., Multiple myeloma. *Nat. Rev. Dis. Primers* **3**, 17046 (2017).
34. S. C. Ling *et al*., Response of myeloma to the proteasome inhibitor bortezomib is correlated with the unfolded protein response regulator XBP-1. *Haematologica* **97**, 64–72 (2012).
35. P. E. Harrington *et al*., Unfolded protein response in cancer: IRE1α inhibition by selective kinase ligands does not impair tumor cell viability. *ACS Med. Chem. Lett.* **6**, 68–72 (2014).
36. S. M. H. Chan, M. P. Lowe, A. Bernard, A. A. Miller, T. P. Herbert, The inositol-requiring enzyme 1 (IRE1α) RNAse inhibitor, 4μ8C, is also a potent cellular antioxidant. *Biochem. J.* **475**, 923–929 (2018).
37. L. Niederreiter *et al*., ER stress transcription factor Xbp1 suppresses intestinal tumorigenesis and directs intestinal stem cells. *J. Exp. Med.* **210**, 2041–2056 (2013).
38. F. Urano *et al*., Coupling of stress in the ER to activation of JNK protein kinases by transmembrane protein kinase IRE1. *Science* **287**, 664–666 (2000).
39. L. Lombardi *et al*., Molecular characterization of human multiple myeloma cell lines by integrative genomics: Insights into the biology of the disease. *Genes Chromosomes Cancer* **46**, 226–238 (2007).
40. R. Ria *et al*., A VEGF-dependent autocrine loop mediates proliferation and capillarogenesis in bone marrow endothelial cells of patients with multiple myeloma. *Thromb. Haemost.* **92**, 1438–1445 (2004).
41. X. Chen *et al*., XBP1 promotes triple-negative breast cancer by controlling the HIF1α pathway. *Nature* **508**, 103–107 (2014).
42. R. Ghosh *et al*., Allosteric inhibition of the IRE1α RNase preserves cell viability and function during endoplasmic reticulum stress. *Cell* **158**, 534–548 (2014).
43. B. C. Cross *et al*., The molecular basis for selective inhibition of unconventional mRNA splicing by an IRE1-binding small molecule. *Proc. Natl. Acad. Sci. U.S.A.* **109**, E869–E878 (2012).
44. H. Rozemuller *et al*., A bioluminescence imaging based in vivo model for preclinical testing of novel cellular immunotherapy strategies to improve the graft-versus-myeloma effect. *Haematologica* **93**, 1049–1057 (2008).
45. T. Iwawaki, R. Akai, S. Yamanaka, K. Kohno, Function of IRE1 alpha in the placenta is essential for placental development and embryonic viability. *Proc. Natl. Acad. Sci. U.S.A.* **106**, 16657–16662 (2009).
46. T. Iwawaki, R. Akai, K. Kohno, IRE1α disruption causes histological abnormality of exocrine tissues, increase of blood glucose level, and decrease of serum immunoglobulin level. *PLoS One* **5**, e13052 (2010).
47. M. Shao *et al*., Hepatic IRE1α regulates fasting-induced metabolic adaptive programs through the XBP1s-PPARα axis signalling. *Nat. Commun.* **5**, 3528 (2014).
48. R. A. Zuellig *et al*., Improved physiological properties of gravity-enforced reassembled rat and human pancreatic pseudo-islets. *J. Tissue Eng. Regen. Med.* **11**, 109–120 (2017).
49. C. Leung-Hagesteijn *et al*., Xbp1s-negative tumor B cells and pre-plasmablasts mediate therapeutic proteasome inhibitor resistance in multiple myeloma. *Cancer Cell* **24**, 289–304 (2013).
50. G. Lu *et al*., The myeloma drug lenalidomide promotes the cereblon-dependent destruction of Ikaros proteins. *Science* **343**, 305–309 (2014).
51. S. Surget *et al*., Cell death via DR5, but not DR4, is regulated by p53 in myeloma cells. *Cancer Res.* **72**, 4562–4573 (2012).